Check for updates

ADVANCED MATERIALS
www.advmat.de

Nanodiamond-Enhanced Magnetic Resonance Imaging

*Jelena Lazovic, Eberhard Goering, Anna-Maria Wild, Peter Schützendübe, Anitha Shiva, Jessica Löffler, Gordon Winter, and Metin Sitti**

Nanodiamonds (ND) hold great potential for diverse applications due to their biocompatibility, non-toxicity, and versatile functionalization. Direct visualization of ND by means of non-invasive imaging techniques will open new venues for labeling and tracking, offering unprecedented and unambiguous detection of labeled cells or nanodiamond-based drug carrier systems. The structural defects in diamonds, such as vacancies, can have paramagnetic properties and potentially act as contrast agents in magnetic resonance imaging (MRI). The smallest nanoscale diamond particles, detonation ND, are reported to effectively reduce longitudinal relaxation time T_1 and provide signal enhancement in MRI. Using in vivo, chicken embryos, direct visualization of ND is demonstrated as a bright signal with high contrast to noise ratio. At 24 h following intravascular application marked signal enhancement is noticed in the liver and the kidneys, suggesting uptake by the phagocytic cells of the reticuloendothelial system (RES), and in vivo labeling of these cells. This is confirmed by visualization of nanodiamond-labeled macrophages as positive (bright) signal, in vitro. Macrophage cell labeling is not associated with significant increase in pro-inflammatory cytokines or marked cytotoxicity. These results indicate nanodiamond as a novel gadolinium-free contrast-enhancing agent with potential for cell labeling and tracking and over periods of time.

1. Introduction

A search for minimally invasive agents with low toxicity and suitability for integrating multiple functions is constantly driving the nanoparticle and nanomedicine research. ND have unique properties, enabling them for multifunctional integration by combining their imaging and biosensing capabilities with drug delivery and cell tracking. NDs have already proven to be effective in drug delivery,[1] gene therapy,[2] bio-sensing,[3] tissue engineering,[4] and bio-imaging.[5] Most of in vivo imaging is conducted using fluorescent NDs,[5] limiting their applications to optical imaging and optically accessible model systems. Whole-body imaging without restrictions imposed by the physical limits of light penetration would be more desirable for most of the clinical applications. Such imaging would enable visualization of complex processes in deep tissues, such as localized on-demand drug and gene delivery, image-guided immune cell tracking and delivery, longitudinal surveillance of cell-based therapies, nanocarriers as well as engineered tissues.

Magnetic resonance imaging (MRI), widely accepted in clinics as a non-ionizing imaging modality capable of deep tissue imaging at high spatial resolution, could be potentially used for direct whole-body imaging and visualization of NDs over long periods non-invasively. At the same time, there is a growing need for an alternative T_1-enhancing contrast agents, as gadolinium-based contrast agents (GBCA) are closely

J. Lazovic, A.-M. Wild
Medical Systems Central Scientific Facility
Max Planck Institute for Intelligent Systems
70569 Stuttgart, Germany

E. Goering
Solid State Spectroscopy Department
Max Planck Institute for Solid State Research
70569 Stuttgart, Germany

P. Schützendübe
Modern Magnetic Systems Department
Max Planck Institute for Intelligent Systems
70569 Stuttgart, Germany

The ORCID identification number(s) for the author(s) of this article can be found under https://doi.org/10.1002/adma.202310109

© 2023 The Authors. Advanced Materials published by Wiley-VCH GmbH. This is an open access article under the terms of the Creative Commons Attribution License, which permits use, distribution and reproduction in any medium, provided the original work is properly cited.

DOI: 10.1002/adma.202310109

A. Shiva
Physical Intelligence Department
Max Planck Institute for Intelligent Systems
70569 Stuttgart, Germany

J. Löffler, G. Winter
Department of Nuclear Medicine
Ulm University Medical Center
89081 Ulm, Germany

M. Sitti
College of Engineering and School of Medicine
Koç University
Istanbul 34450, Turkey
E-mail: sitti@is.mpg.de

M. Sitti
Institute for Biomedical Engineering
ETH Zurich
Zurich 8092, Switzerland

monitored by the U.S. Food and Drug Administration (FDA) due to known cause of nephrogenic systemic fibrosis in kidney patients and unknown long-term consequences of gadolinium tissue deposition, including the brain.[6] A promising emerging alternatives are iron oxide nanoparticles (IONs),[7] especially after advances in surface coating[8] and manufacturing down to single-nanometer,[9] yet they have to find their way back to clinical use.

A direct visualization of NDs was previously achieved by conjugation of amine-functionalized gadolinium ion (Gd^{3+}) to the ND surface.[10] The presence of covalently-attached gadolinium chelates on ND surface led to reduction of longitudinal relaxation time (T_1), however ND without Gd^{3+} did not exhibit significant relaxation properties.[10] Attempts made toward the use of Gd^{3+}-ND conjugates for tumor cell labeling were only partially successful.[11] At high intracellular accumulation, Gd^{3+}-ND conjugates exhibited a negative contrast due to shortening of transverse relaxation time (T_2), diminishing positive contrast due to T_1-shortening, virtually making labeled cells indistinguishable on T_1-weighted images. In addition, for long-term imaging, the toxicity of Gd^{3+}-ND conjugates due to potential release of Gd^{3+} ions, remains a concern. Recently, Overhauser-enhanced MRI (OMRI), is presented as an alternative approach to directly detect and visualize NDs using ultra-low magnetic fields.[12] In the ultra-low magnetic fields, the energy required for in situ hyperpolarization of NDs is in the radio frequency (RF) range allowing in vivo use. In OMRI, the electron spin polarization from the paramagnetic centers in NDs is transferred to ^1H nuclei in the surrounding water. This way the presence of NDs in the solution leads to enhancement in the ^1H MRI signal with contrast sensitive to the ND concentration. The use of ultra-low magnetic field (6.5 mT), however, has a significant drawback for in vivo imaging due to very low signal to noise ratio (SNR), i.e., resolution, inherently associated with low and ultra-low magnetic fields. To take full advantage of MRI-based methods, use of high-field MRI with increased SNR and resolution necessary for theranostic applications and cell tracking is highly desirable.

The occurrence of paramagnetic centers within a diamagnetic nanoparticle presents the unique property of NDs, leading to efficient T_1-signal enhancement without a significant reduction in transverse relaxation time T_2 due to much lower magnetization of NDs. The sparse paramagnetic centers contribute to low transverse over longitudinal relaxivity (r_2/r_1) ratio, making ND particles suitable as T_1-contrast agent. This is very distinctive from superparamagnetic iron oxide nanoparticles (SPIONs), where high concentration of iron ions gives rise to high saturation magnetization, and a significant reduction of transverse relaxation time (T_2). The major advantage of T_1-contrast agents is that their presence is observed as a bright signal enhancement, whereas T_2-contrast agents lead to signal loss and dark areas that can be mistaken for microhemorrhages, calcifications or endogenous iron deposits.[13] We first present T_1- and T_2-relaxation in the presence of detonation nanodiamonds (DND), and then using air-oxidation method, show that both transverse and longitudinal relaxivities can be greatly enhanced (up to 6 times). Present results open opportunities for detonation nanodiamonds (DND) as an efficient T_1-contrast agent in tracking and cell labeling applications, without a concern for Gd^{3+}-toxicity, while utilizing full potential of high-field MRI.

2. Results and Discussion

2.1. Characterization of Detonation Nanodiamonds (DNDs)

Two sets of DNDs were characterized for their potential to reduce T_1 and T_2, as received DNDs obtained from the manufacturer and after air oxidation at 520 °C for 65 min (air-oxidized DNDs). Both DND particles have a crystalline structure, as demonstrated using high resolution transmission electron microscopy (HRTEM) (**Figure 1A,B**), with air-oxidized DND being slightly smaller. Air oxidation presumably reduces the size of NDs (±4 nm/h at 550 °C)[14] and (±3 nm/h at 520 °C);[15] However, only very small reduction in size of DND was observed using HREM and transmission electron microscopy (TEM), Figure S1 (Supporting Information). Using TEM, the average size of commercial DND particles was ≈4.4 nm (similar to the manufacturer's specification) (Figure S1C, Supporting Information), and ≈3.4 nm after air oxidation (Figure S1D, Supporting Information) with occasional bigger size DND particles still present after air oxidation. Nonetheless, air oxidation led to much better dispersion of DND particles (zeta potential -50 mV) and stability in solution as opposed to rapid agglomeration and sedimentation of as received DND (zeta potential 6.4 mV).

The concentration-dependent reduction in longitudinal (T_1) and transverse relaxation time (T_2) were quantified, and corresponding relaxivities were determined from a linear fit. For 7 T longitudinal relaxivity was $r_1 = (1.77\pm0.03)$ [$mM^{-1}s^{-1}$] for DNDs and six times higher for air-oxidized DNDs $r_1 = (11.26\pm0.18)$ [$mM^{-1}s^{-1}$] (Figure 1C). Transverse relaxivity was $r_2 = (6.23 \pm 0.09)$ [$mM^{-1}s^{-1}$] for DNDs and seven times higher for air-oxidized DNDs $r_2 = (47.68\pm1.05)$ [$mM^{-1}s^{-1}$] (Figure 1D) and **Table 1**. Due to much better relaxivities of air-oxidized DNDs and potentially interesting future application, their longitudinal and transverse relaxivities were also measured at 3 T and 14 T, as shown in Figure 1C,D and Table 1. In comparison with gadobutrol, air-oxidized DND had ≈3 times higher longitudinal relaxivity r_1 at all measured field strengths, Table 1. From T_1- and T_2-weighted sets of images it could be seen that air-oxidized DND could perform as dual contrast agent especially at 7 and 14 T, depending on their concentrations, Figure 1E,F.

The ability of the contrast agent to perform well as T_1-contrast agent is mostly dependent on the ratio r_2/r_1; the lower this ratio is, the agent is better suited as T_1-agent. Air-oxidized DNDs had a slightly higher r_2/r_1 ratio (4.1 vs 3.5) compared to the non-oxidized DNDs. To determine if increase in concentration of paramagnetic centers inside air-oxidized DNDs were responsible

Table 1. Transverse and longitudinal relaxivities for DND, air-oxidized DND and gadobutrol for different magnetic field strengths in [$mM^{-1}s^{-1}$].

	r_1 [$mM^{-1}s^{-1}$]	r_2 [$mM^{-1}s^{-1}$]
as received DND, 7 T	1.77±0.03	6.23±0.08
air-oxidized DND, 3 T	18.45±0.85	46.12±0.98
air-oxidized DND, 7 T	11.26±0.18	47.68±1.05
air-oxidized DND, 14 T	9.43±0.16	70.49±2.77
gadobutrol, 7 T	3.91±0.06	5.9±0.04
gadobutrol, 14 T	3.55±0.19	6.62±0.17

© 2023 The Authors. Advanced Materials published by Wiley-VCH GmbH

15214095, 2024, 11, Downloaded from https://onlinelibrary.wiley.com/doi/10.1002/adma.202310109 by Koc University, Wiley Online Library on [23/03/2024]. See the Terms and Conditions (https://onlinelibrary.wiley.com/terms-and-conditions) on Wiley Online Library for rules of use; OA articles are governed by the applicable Creative Commons License

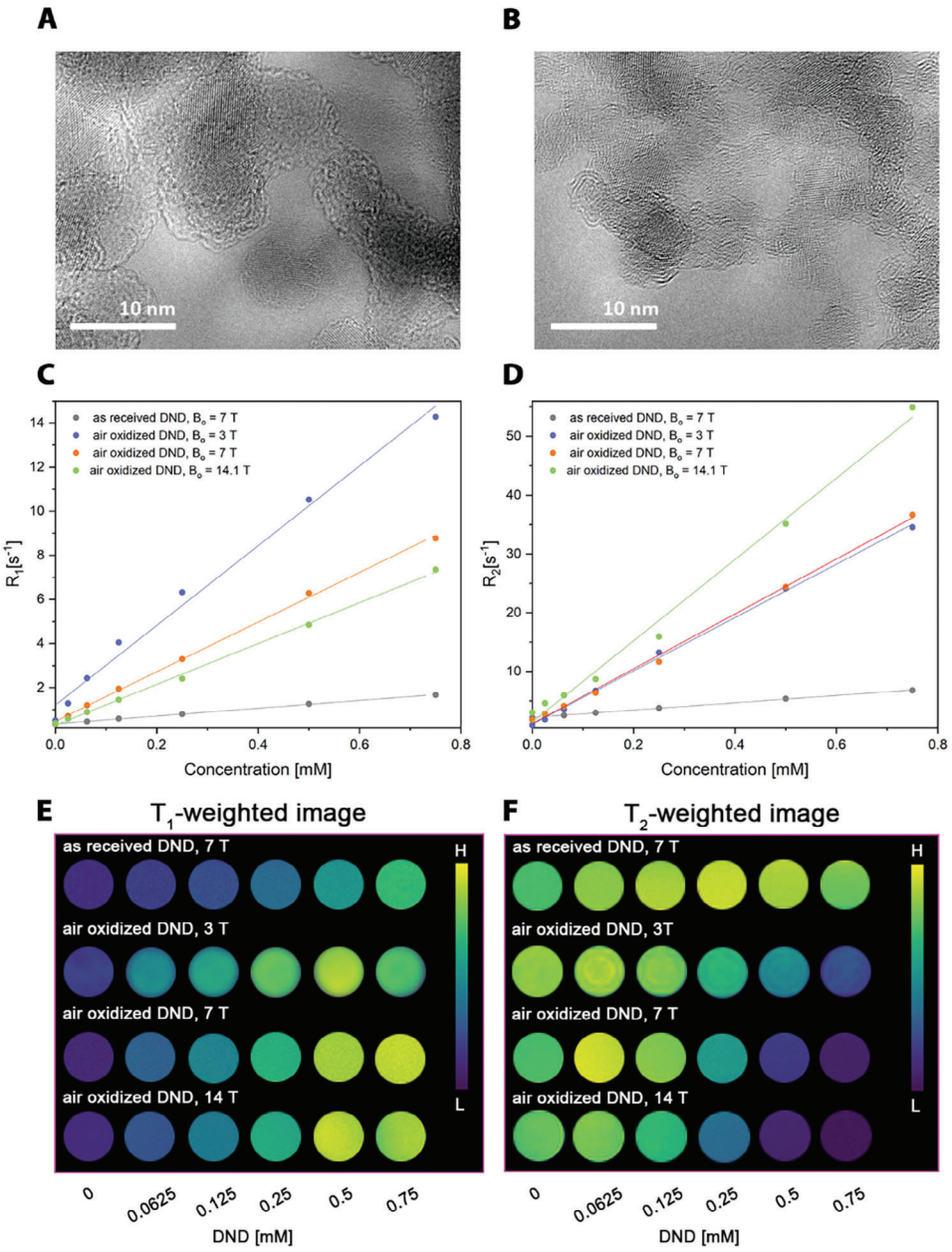


Figure 1. High-resolution transmission electron microscope (HRTEM) images, r_1 and r_2 relaxivity rates, T_1- and T_2-weighted images of as received and air-oxidized DND particle aqueous solutions. A) HRTEM image of as received DND powder showing a crystalline structure of DND particles, and variable particle size (2-7 nm), and B) HRTEM image of air-oxidized DND powder, showing crystalline structure and slightly smaller particles. C) Longitudinal relaxivity rates ($R_1 = 1/T_1$) as a function of the concentration of the DND for 7 T and air-oxidized DND samples for 3 T, 7 T and 14 T magnetic field strengths. D Transverse relaxivity rates ($R_2 = 1/T_2$) as a function of the concentration of the DND particles for 7 T and air-oxidized DND samples for different magnetic field strengths (3 T, 7 T and 14 T). The standard deviation of individual R_1 and R_2 measurements is represented with circles (the actual standard deviation of each measurement is smaller than the outlined circle). E,F) Sets of T_1 (TR/TE 200/6.7 ms) and T_2 (TR/TE 3000/80 ms) -weighted images from different DND aqueous solutions and different magnetic field strengths.

for resulting reduction in T_1 and T_2, superconducting quantum interference device (SQUID) measurements were performed at temperatures from to 2 to 300 K (**Figure** 2A,B). The $M(H)$ curve for 2 K has been fitted by the Brillouin function, assuming a negligible quenched orbital moment and therefore a pure spin g-factor of $g = 2$ has been used. This fit provided us a total angular momentum of $J = 1.1 \pm 0.2$, clearly indicating a microscopic total magnetic moment of $2\mu_B$ as an origin for the observed paramagnetism. The fitted saturation magnetic moment per gram was $m_s = 0.51 \pm 0.03$ emu/g for as received DND and $m_s = 1.2604 \pm 0.03$ emu/g for air-oxidized DND. Using this value, for as received DND, the average magnetic moment per C-atom was calculated as 1.1 $m\mu_B$/C atom. This equals approximately one out of every 2000th ($2\mu_B$/(1.1 $m\mu_B$/C-atom) = 1818) carbon atom sites

© 2023 The Authors. Advanced Materials published by Wiley-VCH GmbH

15214095, 2024, 11, Downloaded from https://onlinelibrary.wiley.com/doi/10.1002/adma.202310109 by Koc University, Wiley Online Library on [23/03/2024]. See the Terms and Conditions (https://onlinelibrary.wiley.com/terms-and-conditions) on Wiley Online Library for rules of use; OA articles are governed by the applicable Creative Commons License

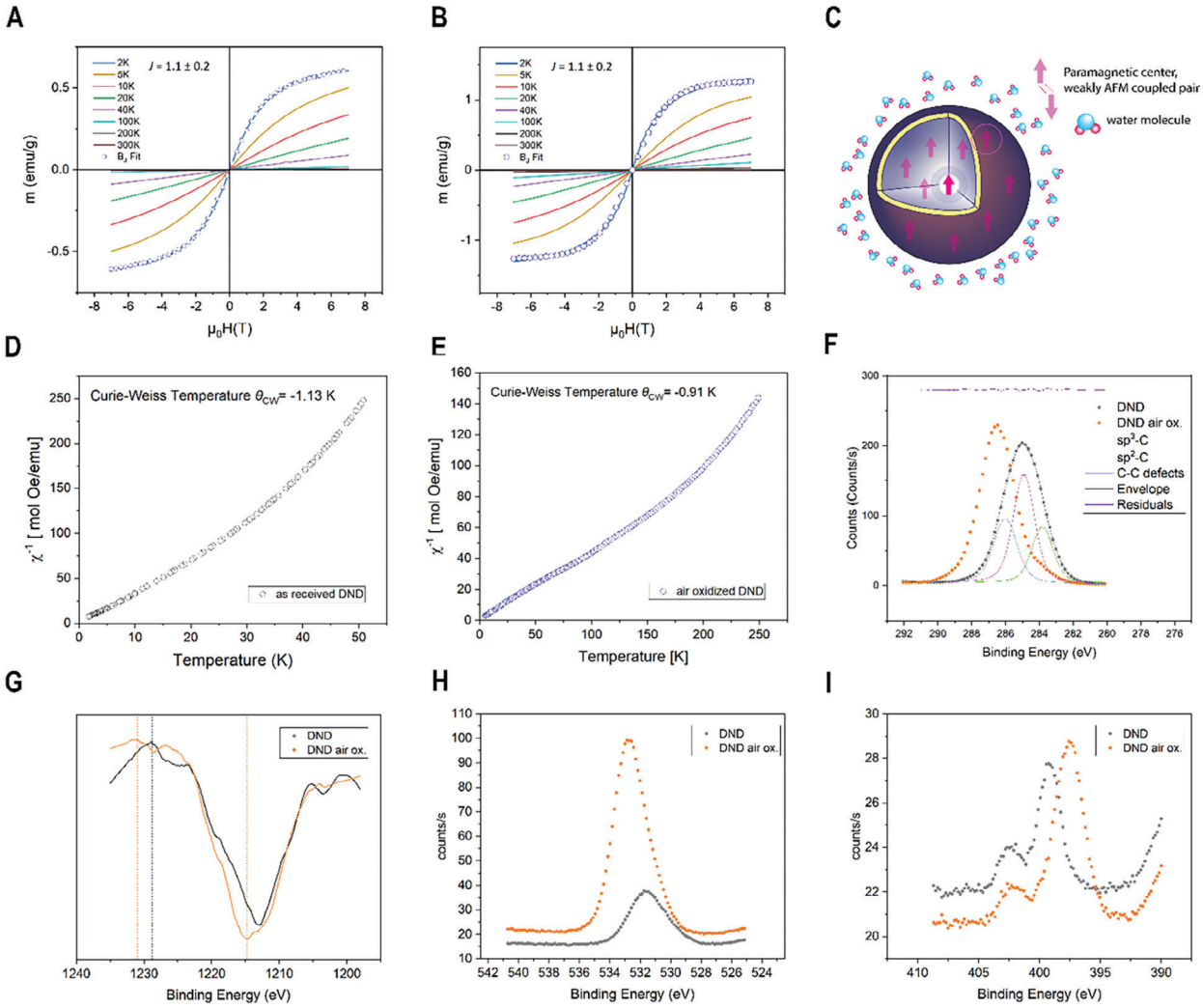


Figure 2. SQUID and XPS characterization of DND particles. A) The $M(H)$ curve for the as received DND sample measured at different temperatures, and calculated J = 1.1 ± 0.2 for 2 K temperature. B) The $M(H)$ curve for air-oxidized DND sample measured at different temperatures, and calculated J = 1.1 ± 0.2 for 2 K temperature. C) Proposed model of DND particle, with random distribution of paramagnetic centers (weakly AFM coupled pair) surrounded by water molecules. D,E) Inverse molar susceptibility versus temperature plots, for calculating Curie-Weiss temperature (Tc = −1.13 K for as received DND (D) and Tc = −0.91 K for air-oxidized DND (E) particles). A small negative value of Curie-Weiss temperature indicates weak antiferromagnetic coupling, and pair of spins with S=½ as the main paramagnetic defects. F) A high resolution C1s XPS spectra with fitted peaks for DNDs, and C1s spectra of air-oxidized DNDs. G) D-parameter, showing first derivative of carbon Auger spectra (C KLL). H) A high resolution O1s XPS spectra of DNDs and air-oxidized DNDs, showing a dominant contribution from C-O and C = O. I) A high-resolution N1s XPS spectra of DNDs and air-oxidized DNDs.

with paramagnetic properties and total spin density of 2.7×10^{19} spin g^{-1}. Similarly, for air-oxidized DND we can calculate average magnetic moment per C-atom to be 2.7 $m\mu_B$/C atom, with increased total spin density (6.6×10^{19} spin g^{-1}) and one out of every 740th carbon with paramagnetic properties. If we take 11 656 as the literature value for number of carbon atoms for a 5 nm DND particle,[16] we can estimate each initial DND will have 6.4 paramagnetic centers on average, while for 4 nm air-oxidized DND there will be 5978 total carbon atoms[16] with 8 paramagnetic centers on average (assuming random distribution).

Previous studies using electron paramagnetic resonance (EPR) estimated the density of most common paramagnetic defects, such as dangling bonds defects (S = 1/2) as high as 1–7 × 10^{19} spin g^{-1}[17] similar to our finding. Paramagnetic centers with triplet state S = 1, such as nitrogen-vacancy (NV^- centers) and double vacancies (V^{2-}) typically have a few orders of magnitude lower abundance.[17c,18] To get information on magnetic ordering of spins, we plotted inverse of molar susceptibility χ^{-1} as a function of temperature and fitted the Currie-Weiss law:

$$\chi^{-1} = \frac{T - \theta_{CW}}{C} \quad (1)$$

as shown in Figure 2D,E. The x-intercept, θ_{CW} is also known as the Curie-Weiss temperature. The presence of weak antiferromagnetic (AFM) interaction of localized spin is similar for both DNDs ($\theta_{CW} < 0$ indicates AFM interaction between

© 2023 The Authors. Advanced Materials published by Wiley-VCH GmbH

15214095, 2024, 11, Downloaded from https://onlinelibrary.wiley.com/doi/10.1002/adma.202310109 by Koc University, Wiley Online Library on [23/03/2024]. See the Terms and Conditions (https://onlinelibrary.wiley.com/terms-and-conditions) on Wiley Online Library for rules of use; OA articles are governed by the applicable Creative Commons License

unpaired electrons), and was previously reported for ultrapure crystalline DND particles.[18] Based on our present findings, we propose a core-shell model, in which paramagnetic centers responsible for increased r_1 relaxivity are randomly distributed throughout the DND particle (Figure 2C) and are in fact weakly AFM coupled pairs with S = 1/2.

Elemental X-ray photoelectron spectroscopy (XPS) analysis revealed DND powder to consist of 93.4% carbon, 3.83% oxygen, 1.92% nitrogen and 0.38% chlorine atoms, while the remaining 0.47% was not determined. Air-oxidized DND powder had 84.16% carbon atoms and increased oxygen to 12.73%, with only a slight increase in nitrogen (2.48%). Purity of as received DNDs was further investigated via inductively-coupled plasma optical emission spectroscopy (ICP-OES). A Fe contamination of ≈0.005 w% was found, while Co, Mn and Ni levels were below the detection limits (<0.0001 w%). This provided a C/Fe atom number ratio of ≈91 000. If Fe would be responsible for the observed paramagnetism, every Fe atom must have a 91 000/2 000 = 45 times higher magnetic moment as observed here which would be ≈90 μ_B. Therefore, we conclude that typical magnetic ion contaminations are not responsible for the measured paramagnetism.

Next, we investigated if paramagnetic centers are located closer to the surface or are evenly- distributed throughout DND particles, and if they are part of sp^3- or sp^2-hybridized carbon atoms. Prior to air oxidation, sp^3-hybridized carbon atoms at 285 eV represented the major content (50%) of DND particle calculated from the fitted peaks. The 285 eV component is characteristic of sp^3-hybridized monocrystalline diamond.[19] Remaining carbon atoms likely belong to distorted carbon-carbon bonds (286 eV), C-O-C (286.9 eV) and C = O (288 eV) bonds,[20] supported by oxygen O1s spectra as well. As a sensitive measure of sp^3- and sp^2-hybridized carbon states, we used the first derivative of the carbon Auger KLL peak, also known as D-parameter.[21] For pure monocrystalline sp^3-hybridized C atoms in diamond D = 14, higher D-values indicate contribution from sp^2-hybridized graphite (e.g., D = 22 for highly-oriented pyrolytic carbon[22]). D-parameters for DND (D = 15.6) and air-oxidized DND (D = 15.7) were similar suggesting mostly sp^3-hybridized carbon states in both cases (Figure 2G), as also evidenced from HRTEM, Figure 1A,B. Following air oxidation, the C1s peak shifted to 286.5 eV with a significantly reduced area ≈284 eV (characteristic of sp^2-hybridized graphite) (Figure 2F). An increase in C-O-C content following air oxidation was evident in O1s spectra with central peak at ≈533 eV, corresponding to C-O-C content overlapping with C = O (531.5-532 eV)[23] (Figure 2H). Both DNDs and air-oxidized DNDs had two nitrogen N1s states. With air oxidation, nitrogen atoms belonging to ≈402.5 eV show almost no change after air oxidation reflecting either their inertness or location within deeper layer of DND.

A slight shift in energy of N1s second peak from 399 to 397.5 eV likely reflects surface oxidation (Figure 2I). It should be kept in mind that Auger electrons are more surface sensitive, therefore their penetration depth is limited to ≈1.1 nm, while C1s, O1s and N1s photoelectrons have higher kinetic energy and an increased penetration depth up to ≈3.3 nm for XPS.[24] In case paramagnetic centers responsible for T_1-reduction were located on the surface among sp^2-carbon atoms, air-oxidized DND would have decreased r_1-relaxivity compared to non-oxidized (due to almost diminished sp^2-carbon peak in air-oxidized DND). Based on D-parameter values and C1s carbon states, it is very unlikely that paramagnetic centers are part of sp^2 hybridization or entirely made up of dangling bonds localized at the interface between the diamond core and outer graphite-like layer as previously suggested.[25] Yet, we cannot rule out a possibility that air oxidation could have created new paramagnetic centers at the surface, since air-oxidized DND have only slightly smaller size. Using theoretical model of outer sphere relaxivity, r_1 -relaxivity increases as square of magnetization (Supporting Information), nonetheless we cannot fully explain six times increase in r_1 for air-oxidized DND.

2.2. Tracking of Air-Oxidized DNDs In Vivo in Chicken Embryos

The T_1-relaxation enhancement in high field (≥7 T) MRI was previously observed with ultra-small superparamagnetic iron oxide nanoparticles (USPIONs).[9,26] DND particles, due to their very low r_2/r_1 ratio, are potentially better suited for high field applications compared to USPIONs. To test whether DNDs can be visualized in vivo, chicken embryos (embryonic development day (EDD) 4) were used. On EDD4, eggs were opened on the side, controls (N = 5) and were not injected, N = 5 eggs were injected with 10 µL of air-oxidized DND aqueous solution (0.25 mM), and N = 5 eggs were injected with 10 µL of gadobutrol solution (16 mM). MRI was performed immediately after the DND particle injection, and repeated after 24, 48, and 96 h (**Figure 3**). To minimize the stress on developing embryos, due to multiple MRIs, only very short scanning sequences (up to 3 min) were used, and total imaging time was kept under 15 min for all embryos. A clear enhancement of the signal on T_1-weighted MR images due to the presence of nanodiamonds is observed with high contrast to noise ratio (CNR = 80) in embryos injected with air-oxidized DND particles (Figure 3B, magenta arrowheads), as compared to control embryos, (CNR = 19, Figure 3A) or embryos injected with gadobutrol (CNR = 22, Figure 3C). Even with short scan times, an enhancement from air-oxidized DND particles could be visualized up to 96 h post injection (Figure 3B). As embryos developed, some signal related to blood flow can be observed (embryos were not cooled down to prevent motion artifacts) in control and gadobutrol injected embryos as well (EED6 and EDD7 as shown in Figure 3A,C). The flow-related enhancement is easily distinguished from DND enhancement based on location and shape. Using inversion recovery (IR) sequences, the background signal can be nulled, providing additional enhancement of DND signal (Figure 3B, last column, magenta arrowheads). For control and gadobutrol injected embryo, T_1-weighted IR images appear noisy, since gadobutrol has diffused out after 96 h, and the tissue signal is mostly nulled in the absence of T_1-contrast agent. This is why signal enhancement is only present in embryos injected with DND particles (Figure 3B, last column). Current images provide strong evidence that signal enhancement from DND particles could be visualized up to 96 h.

2.3. Intravenous Application of Air-Oxidized DND Particles in EDD14 Chicken Embryo

The performance of contrast agents in vivo will ultimately depend on many factors, beside their ability to alter T_1 and T_2 relaxation

© 2023 The Authors. Advanced Materials published by Wiley-VCH GmbH

15214095, 2024, 11, Downloaded from https://onlinelibrary.wiley.com/doi/10.1002/adma.202310109 by Koc University, Wiley Online Library on [23/03/2024]. See the Terms and Conditions (https://onlinelibrary.wiley.com/terms-and-conditions) on Wiley Online Library for rules of use; OA articles are governed by the applicable Creative Commons License

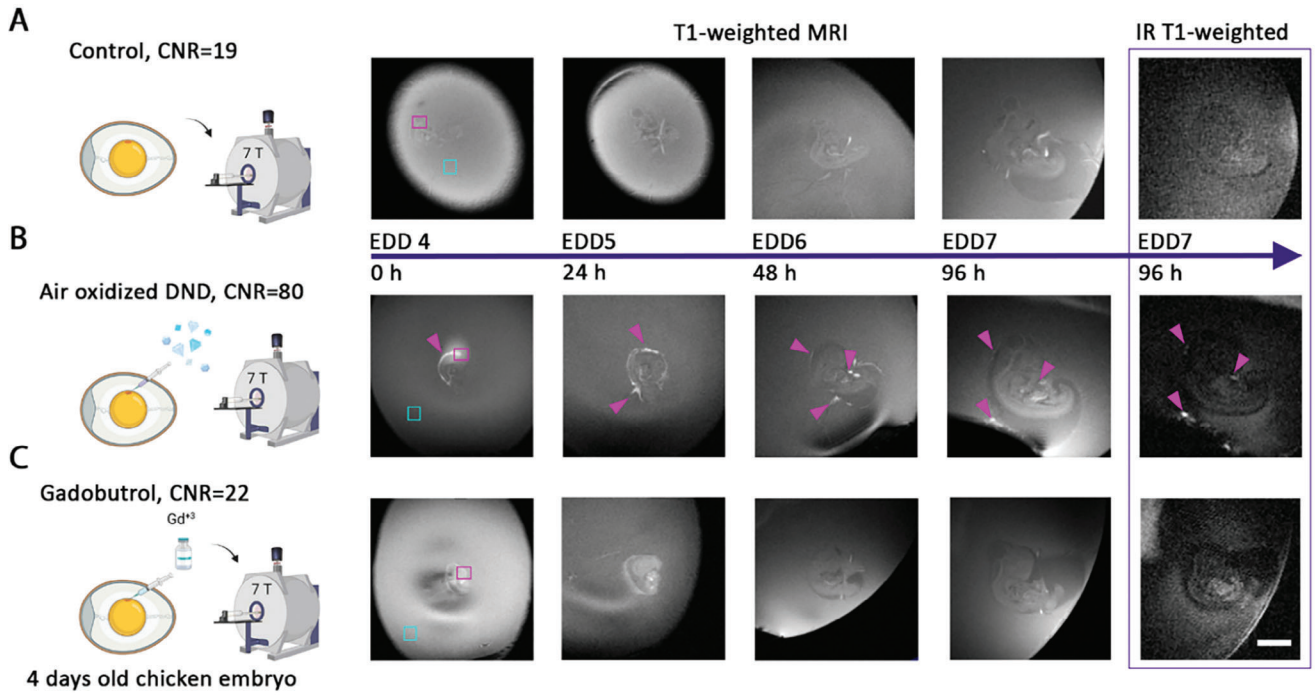


Figure 3. Tracking of air-oxidized DND particles versus gadobutrol over 96 h in early chicken embryo in vivo. Representative T_1-weighted images of chicken embryos from EDD4-EDD7, A) control embryo, no injection, B) embryo injected with air-oxidized DND (10 µL of 0.25 mM), and C) embryo injected with gadobutrol (10 µL of 16 mM). Air-oxidized DND could be followed and visualized up to 96 h (magenta arrowheads) post injection with superior CNR. Magenta squares outline areas of the high signal used for CNR calculations, while cyan squares outline areas of background. Using T_1-weighted inversion recovery (IR) sequence (last column), background signal can be further suppressed to enhance DND signal. Some signal enhancement seen in control or gadolinium injected embryos is due to blood flow, and it can be clearly distinguished based on shape and location from injected DND signal. Scale bar is 5 mm.

times. The major difference, coming from their capability to penetrate vasculature and tissue (small paramagnetic ions, chelated-Gd^{+3}or Mn^{+2}), or remain confined to blood vessels ("blood pool" or intravascular contrast agents), like the most SPIO and USPIO nanoparticles. The air-oxidized DND particles with mean diameter of ≈3.4 nm are on the border between glomerular filtration and capture by the reticuloendothelial system,[27] the downside being that efficient glomerular filtration can potentially lead to reduced plasma circulation. To evaluate potential of air-oxidized DND particles as an intravascular contrast agent in vivo (in ovo) EDD14 chicken embryos were used, where N = 5 embryos served as control (no injection), N = 5 were intravenously injected with 50 µL of 0.625 mM (equivalent to 20 mg kg^{-1} egg) air-oxidized DND particles in citrate solution, and N = 5 were intravenously injected with gadobutrol (Gadavist, 50 µL of 30 mM), and MRI was performed immediately after intravenous (IV) injections. A strong enhancement of the vasculature on T_1-weighted MRI with high CNR is prominent for embryos injected with air-oxidized DND particles (**Figure** 4B, green arrowheads) and especially in second embryo with enlarged cranial veins (Figure 4C, magenta arrowheads), compared to control (Figure 4A) or gadobutrol injected embryos (Figure 4C). These images point the main differences in the performance between air-oxidized DND particles and gadobutrol as the contrast agent. The small gadobutrol molecule is an extravascular contrast agent and provides good tissue enhancement (except the brain tissue, to some extent, due to the intact blood brain barrier), while DND particles are intravascular (blood pool) agents leading to strong vascular enhancement and high CNR of the vasculature. It should be pointed out that flow-related enhancement could not account for increased signal observed in air-oxidized DND particles injected embryos, since cooling them down (to prevent motion artifacts) led to reduced blood flow, as evidenced by the absence of vascular enhancement on MRI of control and gadobutrol injected embryos.

Next, we were interested in investigating if air-oxidized DND particles could lead to tissue contrast enhancement over the next 24 or 48 h. At 24 h post IV injection, both liver (**Figure** 5D, magenta arrowheads) and kidney (Figure 5D, white arrowheads) became prominent and strong signal enhancement was evident. In comparison, no liver or kidney enhancement were present immediately after DND particle IV injection (Figure 5C, green arrowhead) or in control embryo (Figure 5A). This is in contrast to gadobutrol-injected embryos, where after 24 h liver was markedly darker compared to other tissue (Figure 5B, cyan arrowhead). There are few possibilities for the observed liver enhancement at 24 h. The most likely is phagocytosis of blood-circulating DND particles by the reticuloendothelial system, including Kupffer cells in the liver, with actual signal enhancement originating from "labeled" phagocytic cells. A similar mechanism has been already established for SPIONs.[28] The second, less likely possibility is DNDs eventually passing through the vascular endothelium and becoming deposited in the liver parenchyma. In this case, one would expect signal enhancement of the liver in gadobutrol-injected embryos. While there was clear evidence of

© 2023 The Authors. Advanced Materials published by Wiley-VCH GmbH

15214095, 2024, 11, Downloaded from https://onlinelibrary.wiley.com/doi/10.1002/adma.202310109 by Koc University, Wiley Online Library on [23/03/2024]. See the Terms and Conditions (https://onlinelibrary.wiley.com/terms-and-conditions) on Wiley Online Library for rules of use; OA articles are governed by the applicable Creative Commons License

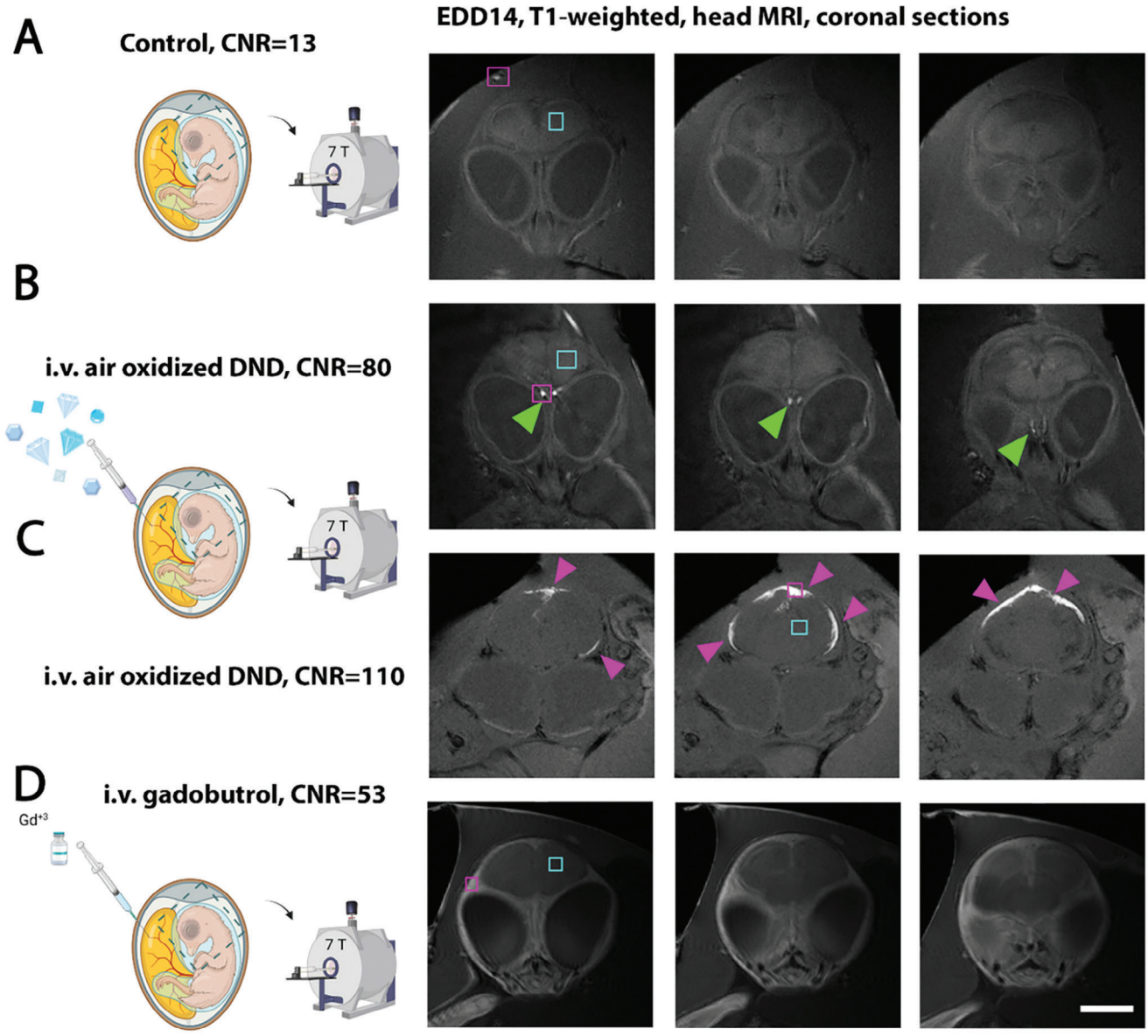


Figure 4. In vivo, in ovo T_1-weighted magnetic resonance (MR) images of intravenous-injected air-oxidized DND particles and gadobutrol. Representative T_1-weigted MR images of the head of A) control chicken embryo (EDD14, no injection), B,C) chicken embryo immediately after iv. injected with air-oxidized DND (50 µL of 0.625 mM solution), D) chicken embryo immediately after iv. injected with gadobutrol (50 µL of 30 mM). Due to particulate nature, DND behaved as a blood pool contrast agent, and led to prominent vascular enhancement, as observed in embryos injected with air-oxidized-DND particles in B (green arrowheads), and more pronounced in C in embryo with enlarged cranial veins (cyan arrowheads). No vascular (flow-related) enhancement in control and gadobutrol animals is seen due to reduced blood flow after cooling down the embryos to prevent motion artifacts. Magenta squares outline areas of high signal used for CNR calculations, while blue squares are background signal (the brain tissue). Scale bar: 5 mm.

enhancement outside the abdomen, the liver was not enhanced (Figure 5B, blue arrowhead). The third possibility is that DND particles are captured by hepatocytes, excreted into the bile and then the intestine, and eventually eliminated through the allantois, as a means of waste material removal in the chicken embryo. The observed enhancement of the liver and the kidneys was reduced at 48 h (Figure 5E), suggesting a mechanism for the elimination of air-oxidized DND particles. While renal clearance is expected to play a role in eliminating smaller DND particles (<10 nm), the hepatic clearance is the predominant route for the excretion of the larger nanoparticles (up to ≈200 nm).[29] Apart from the observed signal enhancements, further studies are necessary to provide direct evidence of the cellular mechanism(s) involved in DNDs accumulation and the elimination.

Taken together, these results offer potential diagnostic value of nanodiamonds, similar to use of SPIONs in cancer diagnostics of liver,[30] where the healthy liver parenchyma would enhance due to presumed phagocytosis of DND by the reticuloendothelial system or hepatocytes, while cancerous tissue void of Kupffer cells

© 2023 The Authors. Advanced Materials published by Wiley-VCH GmbH

15214095, 2024, 11, Downloaded from https://onlinelibrary.wiley.com/doi/10.1002/adma.202310109 by Koc University, Wiley Online Library on [23/03/2024]. See the Terms and Conditions (https://onlinelibrary.wiley.com/terms-and-conditions) on Wiley Online Library for rules of use; OA articles are governed by the applicable Creative Commons License

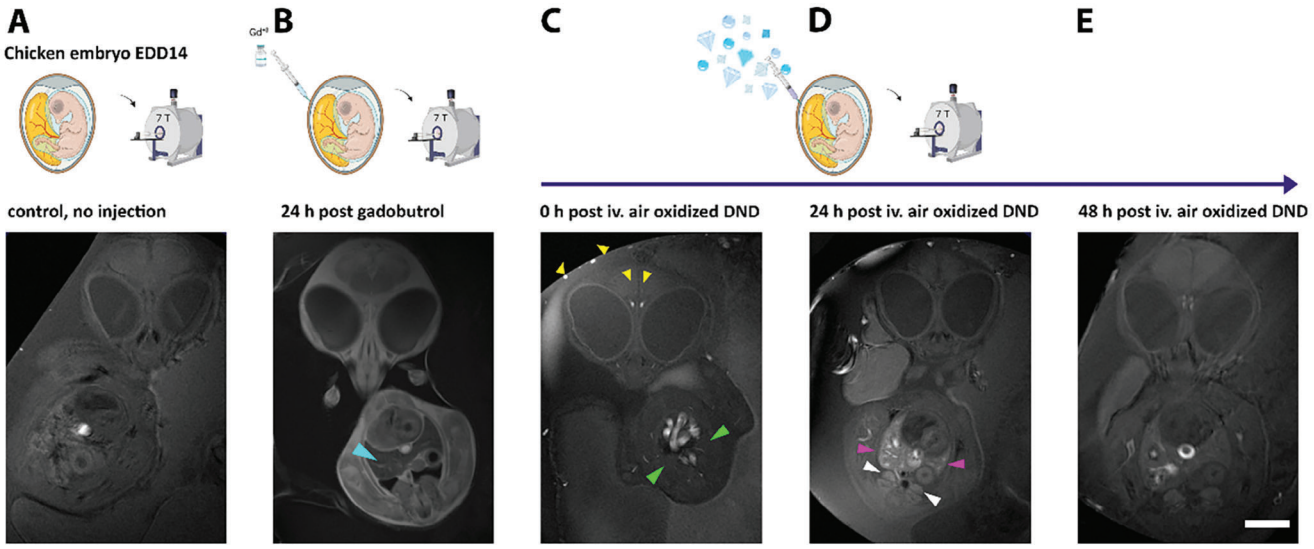


Figure 5. In vivo, in ovo T_1-weighted MR images of intravenous-injected air-oxidized DND particles at 24 h and 48 h after injection. Representative body T_1-weigted MR of A) control chicken embryo (EDD14, no injection), B) chicken embryo 24 h post iv. Gadobutrol (50 µL of 30 mM), cyan arrowhead is pointing to liver. C) Chicken embryo imaged immediately after iv. air-oxidized DND (50 µL of 0.625 mM solution), many blood vessels are immediately enhanced (yellow arrowheads), but not the liver (green arrowheads). D) chicken embryo at 24 h after intravenous injection with air-oxidized DNDs. The liver and kidneys are clearly enhanced (making kidneys noticeable) compared to the embryo 24 h after intravenous injection with gadobutrol, where no liver enhancement was present (cyan arrowhead). E) This enhancement was less pronounced at 48 h in the same embryo. Scale bar: 5 mm.

will not. However, more studies are needed, as well as the kinetics and the clearance associated with potential accumulation of DND particles in tumor tissue impacted by the enhanced permeability and retention effect. Additional applications could include other locations associated with the reticuloendothelial system, such as spleen, kidney, lungs, lymph nodes, and bone marrow, or for visualization of sites of inflammation.

2.4. Macrophage Cell Labeling with Air-Oxidized DND Particles

To confirm that phagocytic cells can be indeed labeled with DND particles and visualized as bright signal on T_1-weighted images, in vitro labeling of murine macrophages was performed next. Non-invasive cell labeling based on T_1-contrast enhancement could greatly improve cell tracking in vivo and overcome many shortcomings associated with the use of T_2-contrast agents for cell labeling. MRI in combination with DND-labeled immune cells could be used for visualization of inflammation, tumor infiltration, immune cell tracking and homing, and for image-guided drug/cell delivery. In contrast to SPION contrast agents, where T_2-relaxation is dominating, inducing perturbation of the surrounding magnetic field and signal loss,[31] DND particles show increased signal and positive T_1-contrast enhancement enabling them to be unambiguously distinguishable on T_1-weighted images. Cell labeling with T_2-contrast agents still has the highest sensitivity, however, labeled cells are virtually indistinguishable from endogenous iron, ferritin, and hemosiderin deposits, thus complicating interpretation of tracking results. To overcome false positive detection associated with negative contrast agents, in the past, ^{19}F-labeling with perfluorocarbon nanoemulsions was used,[32] although with lower sensitivity but much higher specificity. Another proposed alternative was labeling cells with chemical exchange and saturation transfer (CEST) contrast agents[33] with an order of magnitude lower sensitivity.[34]

To in vitro confirm that air-oxidized DND particles could be used for efficient immune cell labeling, murine macrophage cell cultures were incubated with air-oxidized DNDs (1.25 µM and 2.5 µM) for 24 h. Following incubation, labeled and control macrophages were passed through a 1-µm diameter membrane to allow filtering of DND particles that have not been uptaken. Additionally, to rule out that air-oxidized DND might attach to the membrane, 25 µM solution of air-oxidized DND was passed through the same 1-µm membrane. All membranes embedded in agarose gel were imaged using high-resolution T_1-weighted MRI. No signal enhancement on the membrane was found for the control groups (air-oxidized DND and unlabeled macrophages, **Figure** 6C,D), while areas of hyperintense signals were found on the membrane containing air-oxidized DNDs-labeled macrophages: 1.25 µM (Figure 6E) and 2.5 µM (Figure 6F). Based on the number of macrophages that should be present on the membrane, we estimated each point of signal enhanced area to be 1 000 or less macrophages. To confirm that macrophages were indeed labeled with DNDs, SEM imaging of macrophages following 24 h incubation with 1.25 µM DNDs was performed, as well as live cell confocal imaging after 24 h incubation with fluorescein isothiocyanate–dextran (FITC-dextran) coated DND particles and FITC-dextran only. Phagocytosis of free DNDs particles is captured by SEM (Figure 6B) along with neighboring DND-containing macrophages. During incubation in cell culture media, we noticed that air-oxidized DND tend to form aggregates (as visible from the SEM image, Figure 6B) that precipitate to the bottom of the cell culture plate. The aggregation might be favorable for the phagocytosis, and for T_1-weighted imaging as well, since aggregated DND will provide more enhancement due to higher local concentration.

© 2023 The Authors. Advanced Materials published by Wiley-VCH GmbH

15214095, 2024, 11, Downloaded from https://onlinelibrary.wiley.com/doi/10.1002/adma.202310109 by Koc University, Wiley Online Library on [23/03/2024]. See the Terms and Conditions (https://onlinelibrary.wiley.com/terms-and-conditions) on Wiley Online Library for rules of use; OA articles are governed by the applicable Creative Commons License

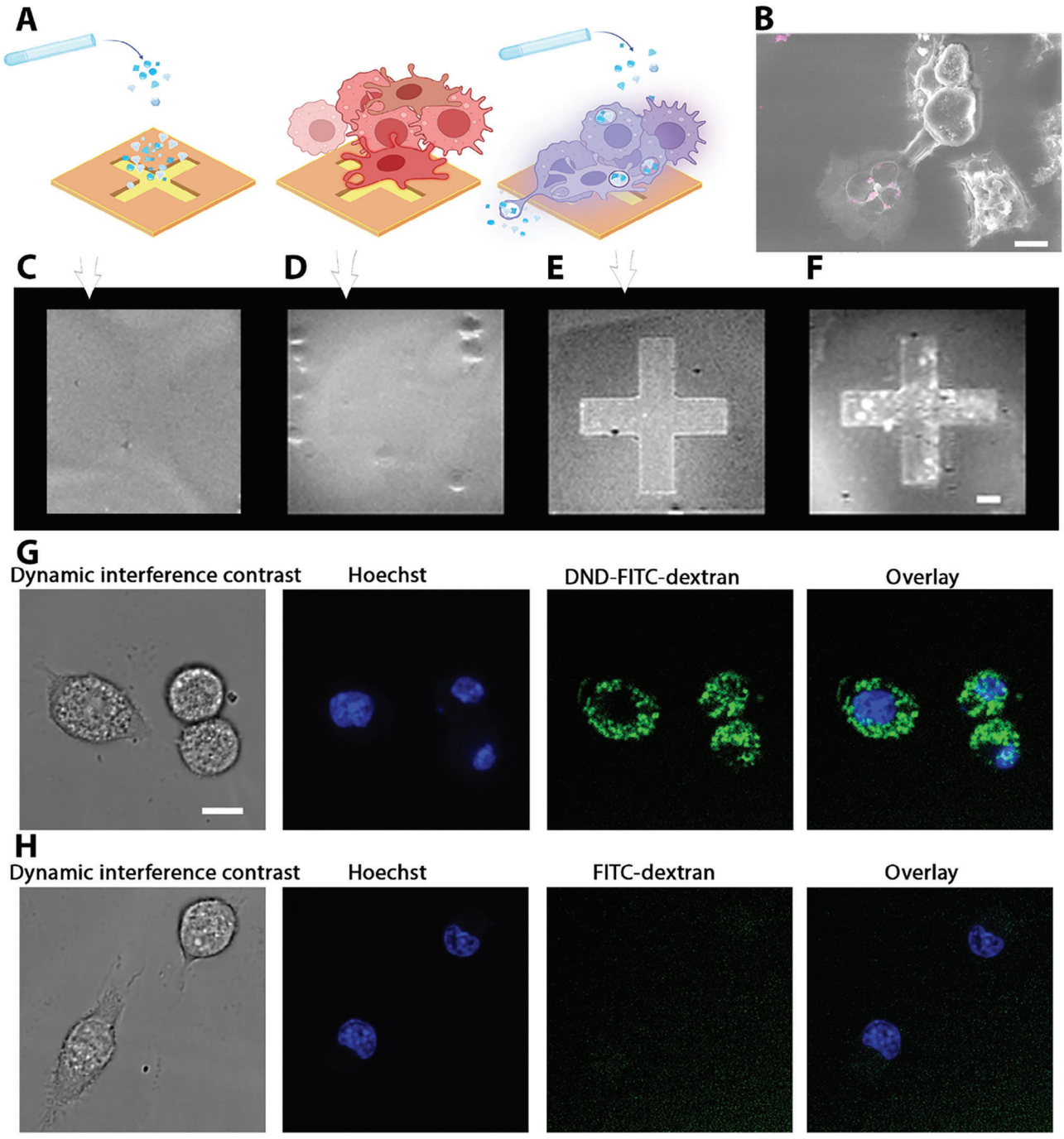


Figure 6. Macrophage cell labeling in vitro using air-oxidized DNDs and visualization using T1-weighted MRI. Top row, from left to right: A) schematic illustrations of the air-oxidized diamonds on the membrane (without macrophages), with macrophages, and air-oxidized DND-labeled macrophages. B) SEM image of the macrophages incubated with air-oxidized DNDs (1.25 µM) with phagocytosis of the DND particles; scale bar: 10 µm. Air-oxidized DND clusters are pseudo colored as pink. To aid visualization of labeled cells, each membrane was covered with tape except the cross-shaped area that was left uncovered. To separate DND particles that have not been uptaken, labeled macrophages were strained using a 1 µm membrane. Bottom row: T1-weighted MR images (the maximum intensity projection of two neighboring slices) of the membranes embedded in agarose with air-oxidized DND (C), unlabeled macrophages (D), macrophages labeled with 1.25 µM air-oxidized DND (E) and macrophages labeled with 2.5 µM air-oxidized DND (F). Contrast achieved with DND-labeled macrophages is readily visible as highlighted cross-shaped area even for lower DND concentration (1.25 µM), E. This bright contrast was absent for air-oxidized DND as they likely passed through the membrane and unlabeled macrophages (C, D)). A clusters of macrophages labeled with higher DND concentration (2.5 µM) can be readily seen as bright dots F). Based on the cell count we can estimate that each membrane had 300 000 – 400 000 cells, and each cluster in F to have ≈1 000 or less labeled macrophages, 1 mm scale bar. G) Confocal imaging of live murine macrophages incubated for 24 h with FITC-dextran coated DND, with evident FITC-fluorescence inside the macrophages. H) murine macrophages incubated for 24 h with FITC-dextran only, notice absence of FITC-fluorescence. Scale bar is 10 µm.

© 2023 The Authors. Advanced Materials published by Wiley-VCH GmbH

15214095, 2024, 11, Downloaded from https://onlinelibrary.wiley.com/doi/10.1002/adma.202310109 by Koc University, Wiley Online Library on [23/03/2024]. See the Terms and Conditions (https://onlinelibrary.wiley.com/terms-and-conditions) on Wiley Online Library for rules of use; OA articles are governed by the applicable Creative Commons License

Using fluorescent FITC-dextran coated DND particles, we provide additional evidence for the intracellular uptake of FITC-dextran-DND particles by macrophages (Figure 6G). On the other hand, no labeling was observed when macrophages were incubated with FITC-dextran only (Figure 6H). Due to its high molecular weight, FITC-dextran is not capable of permeating the cellular membrane, yet it is below the size limit for the phagocytosis by macrophages.

These results, including in vivo phagocytosis by reticuloendothelial cells, strongly argue for the role of air-oxidized DND in future cell tracking applications in vivo. Even more interesting might be the use of fluorescent (NV^- centers containing) NDs as a dual mode imaging agent. Based on our results, it is likely that these NDs could be tuned to have T_1- or T_2-signal enhancing properties, enabling multimodal fluorescent and MR imaging.

2.5. Cytotoxicity and Immunogenicity

Prior to any in-vivo application of DND particles, safety assessments such as cytotoxicity and immunogenicity are imperative. Previous, comprehensive biocompatibility assessment of DND in non-human primates and rats found dosage up to 25 mg kg^{-1} to be well tolerated without any organ dysfunction or significant pathological findings upon histology.[35] Toxicity studies on neuronal and lung cell lines found no evidence of a reactive oxygen generation or mitochondrial membrane disruption at high (up to 2.5 μM equivalent to 0.1 mg mL^{-1}) DND concentrations, suggesting their suitability in biomedical applications.[36] In comparison with other carbon nanomaterials, such as single- and multi-walled carbon nanotubes, carbon black, detonation DND exhibited the least cytotoxicity especially when incubated with macrophages.[36] The macrophages might be especially vulnerable to nanoparticles due to their innate immune response to foreign material. Using LIVE/DEAD staining kit we examined cytotoxicity at 24 and 48 h in macrophages following incubation with 2.5 μM equivalent to 0.1 mg mL^{-1} and 1.25 μM equivalent to 0.05 mg mL^{-1} air-oxidized DND concentrations, **Figure** 7B,C. The LIVE/DEAD stains live and dead cells directly, excluding a possibility for DND interference with absorbance used in colorimetric assays such as WST-8/CCK8. Direct cell counting revealed ≈5-8% dead cells following 2.5 μM DND treatment at 24 and 48 h and following 1.25 μM DND treatment at 48 h. Control cells as well as 1.25 μM DND treated group at 24 h had less than 3% dead cells. These results are in accord with the previous assessment of DND toxicity using MTT assay.[36] Cytokines released in response to 1.25 μM and 2.5 μM DND were measured using a cytometric bead array analysis of macrophages. Cytokines directly secreted by macrophages involved in an innate immune response (TNF-α, IL-6, IL-10), and activation of neutrophils (IL-17-α) were measured at 24 and 48 h post DND or LPS incubation. Other cytokines involved in immunoregulation, but not directly secreted by macrophages, IL-2 and IL-4 were measured as internal control. The only significant ($P < 0.05$) increase in cytokines compared to control group (2-way ANOVA, with Bonferroni post hoc test) was in response to LPS at 24, 48 and 72 h (IL-6 and TNF-α) and in response to LPS at 72 h only (IL-10), Figure 7A. Therefore, for the time points of examined cytokine response, no immunogenicity with air-oxidized DND treatment up to 2.5 μM was observed, Figure 7A.

3. Conclusions

The presence of paramagnetic centers within small diamagnetic DND particles enables their efficient detection on T_1-weighted MRI images at biologically-relevant concentrations without the need for conjugation with gadolinium or use of hyperpolarization techniques, simplifying both detection and manufacturing processes. Our initial results establish both tracking and cell labeling capabilities in vivo, without marked toxicity or immunogenicity, opening venues for nanodiamonds in design of image-guided, on-demand, cell- and nanocarrier-based targeted delivery systems. Such systems are already envisioned as disruptive solutions to circumvent many unwanted side effects associated with systemic administrations. A combination of clinically-relevant, non-invasive and whole-body imaging technologies, such as MRI, with minimally-toxic agents, such as ND particles, offers a powerful approach toward this vision. Direct visualization of DND particles with high CNR, opens new possibilities for unambiguous tracking, devoid of many shortcomings associated with labeling with negative contrast agents. Together with recent developments in fluorescent NDs, it might become possible to take advantage of both optical and MR imaging modalities, achieving very high spatial resolution in combination with deep tissue imaging.

4. Experimental Section

Materials: DND nanoparticles (>98.3% pure, size range 3–10 nm) were purchased from US Research Nanomaterials, Inc (Houston, TX USA). Air-oxidized DNDs were obtained by heating DND powder in air at 520 °C for 65 min using a furnace (Grodke GmbH, Germany). Lipopolysaccharides (LPS), FITC-dextran (70 000 MW), low melting agarose, gadobutrol monohydrate, citric acid, and sodium citrate were purchased from Sigma Aldrich (Germany). NucBlue was purchased from Invitrogen. For in vivo injection, Gadovist (gadobutrol solution) was purchased from Bayer (Germany). The murine monocyte-macrophage cell line J774A.1 (TIB-67, ATCC, USA) and murine fibroblast NIH/3T3 (CRL-1658, ATCC, USA) were used. Cytokines (interleukin (IL)−2, IL-4, IL-6, IL-10, IL-17α, IFN-γ, TNF-α) were purchased as a mouse Th1/Th2/Th17 cytokine kit from BD Bioscience (USA). Specific pathogen free (SPF) fertilized eggs were purchased from Valo Biomedia GmbH, Germany. Ultrasonic cleaner (USC-THD) from VWR (Germany) was used for all sonications and performed better than high power sonicators.

FITC-Dextran Coating of DND Particles: FITC-dextran was diluted in ddH_2O (2 mg mL^{-1}) and added to 2 mg mL^{-1} air oxidized DND as 1:10 ratio. The mixture was heated to 50 °C for 20 min.

Cell Cultures: Murine monocyte-macrophage cells (J774A.1) and murine fibroblast cells lines (NIH/3T3) were incubated in Dulbecco's modified Eagle's medium (DMEM, Gibco, Thermo Fisher, USA) supplemented with 10% fetal bovine serum (Gibco) and 1% penicillin streptomycin mixture (Gibco, Gibco, Thermo Fisher, USA) at 37 °C in fully-humidified air containing 5% CO_2. The cells were passaged after reaching 80 % confluency and used before passage number 15.

Transmission Electron Microscopy (TEM), High Resolution Tem (HRTEM), Confocal Microscopy, and Dynamic Light Scattering (DLS): TEM was performed on Philips CM200 transmission electron microscope using an accelerating voltage of 200 kV. The sample was prepared by dropping 1 microliter of DNDs suspended in ddH_2O on a

© 2023 The Authors. Advanced Materials published by Wiley-VCH GmbH

15214095, 2024, 11, Downloaded from https://onlinelibrary.wiley.com/doi/10.1002/adma.202310109 by Koc University, Wiley Online Library on [23/03/2024]. See the Terms and Conditions (https://onlinelibrary.wiley.com/terms-and-conditions) on Wiley Online Library for rules of use; OA articles are governed by the applicable Creative Commons License

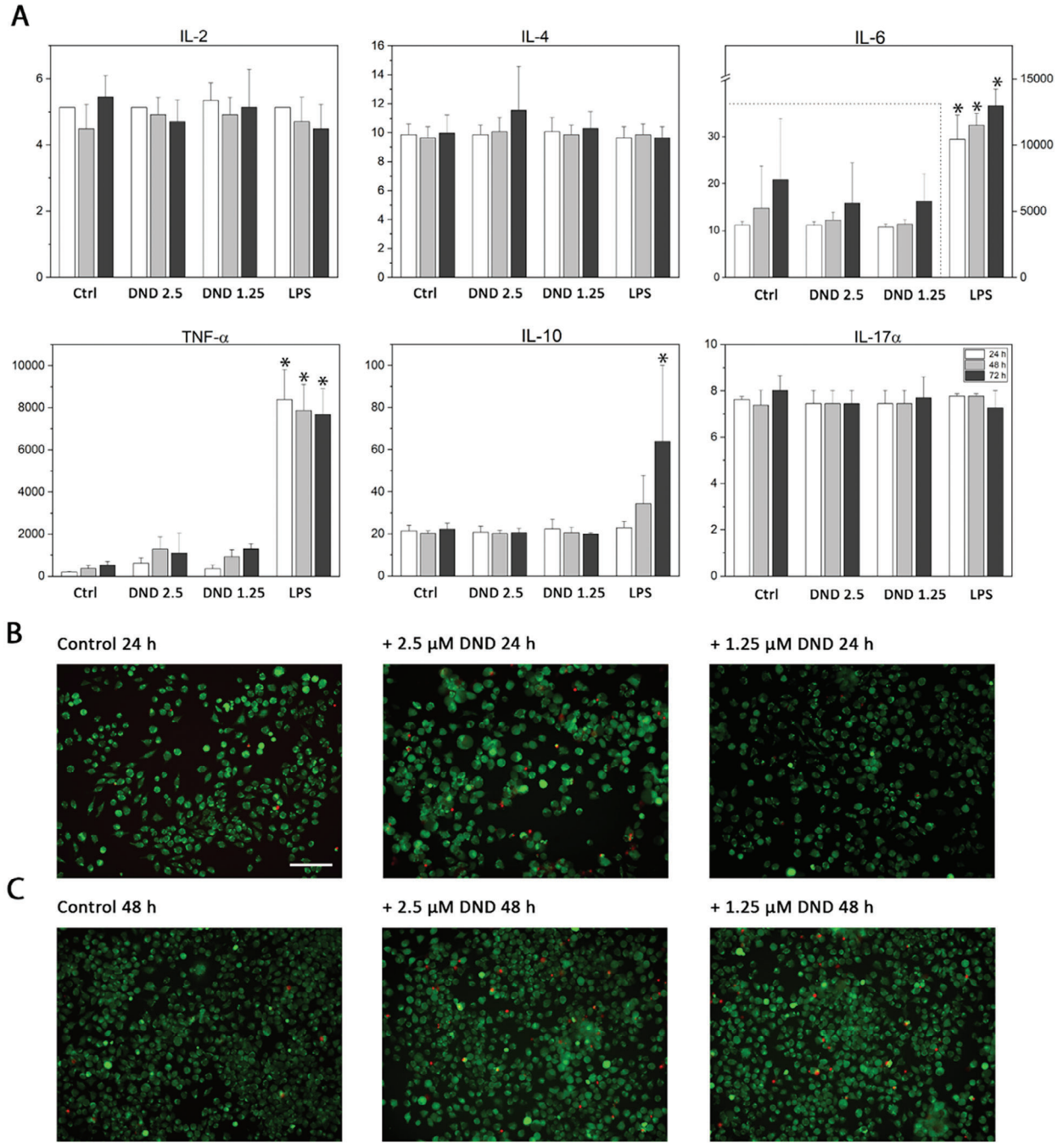


Figure 7. Cytotoxicity and immunogenicity evaluation of air-oxidized DND using macrophage cell cultures. A) A quantification of various cytokines produced by macrophages in response to 2.5 μM air-oxidized DNDs and 1.25 μM air-oxidized DNDs, and 0.1 μg mL^{-1} LPS at 24, 48, and 72 h as measured by the CBA assay. A) statistically significant increase in IL-6 and TNF-α was noticed only in response to LPS treatment (two-way ANOVA, followed by Bonferroni post-hoc test ($P < 0.05$). B) LIVE/DEAD staining of control macrophages incubated with media only; macrophages incubated with 2.5 μM air-oxidized DNDs and 1.25 μM air-oxidized DNDs at 24 h. Scale bar: 50 μm. C) LIVE/DEAD staining of control macrophages incubated with media only; macrophages incubated with 2.5 μM DNDs and 1.25 μM DNDs at 48 h. Macrophages incubated with DNDs had between 5–8% dead cells compared to 3% among control groups, based on cell counting.

copper grid (Plano GmbH, Germany). HRTEM was performed on advanced TEM (JEOL ARM200F, JEOL Co Ltd.) using an accelerating voltage of 200 kV and carbon lacey grid (Agar Scientific, United Kingdom). The sample was air dried prior to imaging. Live cell confocal imaging was done using spinning disk Nikon confocal microscope (Nikon Ti-E). DLS was done using Litesizer 500 (Anton Pear, Germany).

Sample Preparation and Scanning Electron Microscopy (SEM): Mouse macrophages (≈150000 cells) were cultured on an 18 mm round glass coverslips inside a 12-well plate and incubated with 1.25 μM DNDs added to

© 2023 The Authors. Advanced Materials published by Wiley-VCH GmbH

15214095, 2024, 11, Downloaded from https://onlinelibrary.wiley.com/doi/10.1002/adma.202310109 by Koc University, Wiley Online Library on [23/03/2024]. See the Terms and Conditions (https://onlinelibrary.wiley.com/terms-and-conditions) on Wiley Online Library for rules of use; OA articles are governed by the applicable Creative Commons License

cell culture media. After 24 h, samples were triple washed with PBS and incubated in 4% formaldehyde at room temperature for 20 min. Afterward, samples were triple washed with PBS and dehydrated in sequentially increasing ethanol concentrations (30%, 50%, 70%, 80%, 90%, 100%) for 5 min each followed by ethanol:hexamethyldisilazane solutions (2:1, 1:1, 1:2, 0:1) for 10 min each. Prepared slides were air dried and mounted on the SEM sample holder. SEM was performed on Zeiss Ultra 550 Gemini scanning electron microscope (Carl Zeiss GmbH, Germany) using an accelerating voltage of 10 keV and variable-pressure secondary electron (VPSE) detector.

SQUID Measurements and Coupled Plasma Optical Emission Spectroscopy (ICP-OES): Magnetometry data was measured by Quantum Design MPMS3 SQUID VSM magnetometer in DC mode. To approximate the diamagnetism for as received DND, the small room temperature negative slope of −0.006915 emu/g/T has been determined by fitting the 300K $M(H)$ curve, and −0.01135 emu/g/T for air-oxidized DND. As usual for diamagnetism correction, this small negative slope has been subtracted from all $M(H)$ curves. Coupled plasma optical emission spectroscopy was characterized using a Spectro Ciros CCD ICP-OES instrument (Spectro Analytical Instruments GmbH, Germany).

X-Ray Photoelectron Spectroscopy (XPS): XPS measurements were carried out in a Thermo VG Thetaprobe system (Thermo Fisher Scientific, USA) employing monochromatic Al Kα/ X-ray radiation ($h\nu$ = 1486.7 eV) produced with an electrical power of 100 W. The X-ray spot size on the sample was ≈400 µm in diameter. A flood gun was employed to compensate possible surface charging. No further correction of peak position was conducted. The base pressure of the used XPS was 8×10^{-10} mbar. Survey spectra were recorded with a pass energy of 200 eV and a more detailed spectra of single elemental peaks were measured in snapscan mode afterward except for the Auger peak of C KLL spectrum which was measured in scan mode. The measurements were fitted using the fitting routines included in the XPS software Advantage. Derivative spectra were obtained using the Savitzky-Golay smoothing and second-order polynomial. D-parameter was calculated as a distance between most positive maximum and most negative minimum of the first derivative.[21] Curve integration in Origin (OriginPro, Origin Lab Coorporation, USA) was used to estimate sp^3-hybridized state of carbon atoms (diamond) content from fitted peaks for as received versus air-oxidized DNDs.

Quantification of Longitudinal and Transverse Relaxation Times T1 and T2: To calculate longitudinal (T_1) and transverse (T_2) relaxation times, six different concentrations of DNDs and air-oxidized DNDs were prepared (0.025, 0.0625, 0.125, 0.25, 0.5, 0.75 mM) in double-distilled water. While T_1 and T_2 were quantified for air-oxidized DND at 3 T, 7 T and 14 T, quantification of T_1 and T_2 for as received DND was done only fat 7 T. Prior to preparation of final solutions, as received DND powder and air-oxidized DND powder was extensively sonicated (≈10 h, followed by 2 × 1 h centrifugation at 20 000 g and resuspension) to break down agglomerates and aid more stable particle suspension. Final solutions were transferred into a 1 mL syringes for MRI. For measurements at 3 T magnetic field, Siemens Prisma MRI system (Siemens, Germany). Turbo spin echo sequence with variable repetition (TR = 60, 70, 80, 90, 100, 200, 300, 400, 500, 600, 700, 800, 900, 1000, 2000, 3000, 4000, 5000, 6000, 7000, 8000 ms) and fixed echo time (TE = 10 ms), turbo factor = 2, 350 × 350 µm^2 in plane resolution, 1 mm slice thickness, number of experiments (NEX) = 1, was used for T_1 quantification. A spin echo, multi-echo sequence with fixed TR = 8 000 ms and 32 variable TE times (11-352 ms), 350 × 350 µm^2 in plane resolution, slice thickness 1 mm, NEX = 1 was used for T_2 quantification. For 7 T measurements, Bruker preclinical scanner (Bruker, Germany) and 40 mm quadrature birdcage coil were used. Longitudinal relaxation time (T_1) was measured using a saturation recovery method with a variable repetition time and rapid acquisition with relaxation enhancement (RAREVTR); TR = (60,70, 80, 90, 100, 200, 300, 400, 500, 600, 700, 800, 900, 1000, 2000, 3000, 4000, 5000, 6000 ms), and fixed echo time (TE) = 6.68 ms, RARE factor = 2, 117 × 117 µm^2 in-plane resolution, 1 mm slice thickness, NEX = 1. Transverse relaxation time (T_2) was measured using single slice multi-echo spin echo sequence with fixed repetition time TR = 3 000 ms and 30 echo times (TE = 5.4–162 ms), 150 × 150 µm^2 in-plane resolution, 1 mm slice thickness, NEX = 2. Measurements of relaxation times at 14 T were done using Bruker preclinical scanner (Bruker, Germany). RAREVRT sequence with variable repetition time TR = (60,70, 80, 90, 100, 200, 300, 400, 500, 600, 700, 800, 900, 1000, 2000, 3000, 4000, 5000, 6000 ms), fixed TE = 5.58 ms, 140 × 140 µm^2 in-plane resolution, 1 mm slice thickness, NEX = 1 was used to quantify T_1, while T_2 was quantified using single slice spin echo multi-echo sequence with fixed TR = 3 000 ms, and 30 variable echo times (TE = 4.69-140.7 ms), 175 × 175 µm^2 in-plane resolution, 1 mm slice thickness, NEX = 1. Image processing and parameter fitting ($R_{1,2}$ and $T_{1,2}$) was done offline using ImageJ (National Institutes of Health; imagej.nih.gov/ij/) and the MRI analysis calculator plugin written by Karl Schmidt. To determine longitudinal and transverse relaxivities $r_{1,2}$, the linear regression was done in Origin using Equation 2 $R_{1,2}$ *are experimentally measured longitudinal and transverse relaxivity rates*, $R^o{}_{1,2}$ are longitudinal and transverse relaxivity rates of the solvent (deionized water), and [*ND*] is concentration of ND in mM:

$$R_{1,2} = R^o_{1,2} + r_{1,2}\,[ND] \tag{2}$$

Preparation of Sodium Citrate Air-Oxidized DND Solution for In Ovo Injections and iv. Injections: To prevent rapid agglomeration of DND in the blood, sodium citrate solution (pH 7.0) with air-oxidized DND was prepared by adding 12.1 mg of sodium citrate and 3.358 mg of citric acid to 1 mL of ddH_2O and adjusting the pH to 7.0. Afterward, sodium citrate solution was added to 0.75 mM air-oxidized DND in ddH_2O (1:2) and sonicated for 4 h, followed by centrifugation at 5 000 g for 10 min to remove bigger agglomerates, and sterile filtered using (0.22 µm syringe filter).

Ethical Statement for Use of In Ovo Chicken Embryo Model: All chicken embryo experiments were done according to current German law, where no approval or notification of animal experiments are needed if birds are used before hatching (TierSchVersV § 14.2. valid until 12/2023). All chicken embryos have been sacrificed by embryo development day (EDD) EDD17 the latest.

In Ovo Chicken Embryo Model EDD4-EDD7: Fertilized chicken eggs were incubated using Rcom pro 20 incubator program for chicken (Rcom Incubators, USA). EDD0 was the day incubation started. On EDD4 eggs were candled to locate the embryo, placed on the side, and just above the embryo an opening ≈7 × 7 mm was cut using a diamond cutter. Under a microscope, EDD4 embryos, were injected with air-oxidized DND solution (10 µL of 0.25 mM solution) N = 5, or with 10 µL of 16 mM gadobutrol solution, N = 5, and N = 5 control eggs were not injected. The openings were sealed with parafilm. MRI was performed after the injections were done, and at 24 h, 48 h and 96 h post injection. A T_1-weighted gradient recalled echo sequence was used (TR/TE = 100/4 ms, 200 × 200 µm^2 in-plane resolution, 1 mm slice thickness, NEX = 2, 1 min total imaging time), and T_1-weighted fast imaging with steady state precession in free induction decay mode (TR/TE = 5.57/2.77 ms, 300 × 300 µm^2 in-plane resolution, 1 mm slice thickness, NEX = 16, 2 min 24 s total imaging time) with 280 ms duration inversion pulse. Contrast to noise ratio (CNR) is defined as difference of signal intensities (SI) from two areas divided by standard deviation (SD) of the noise, Equation 3:

$$CNR = \frac{SI\,(1) - SI\,(2)}{SD_{noise}} \tag{3}$$

In Ovo Chicken Embryo Model EDD14: On EDD4 the blunt end of the egg was cut with a diamond cutter, the membrane was carefully removed, the opening was sealed with parafilm and the egg was placed back into the incubator until EDD14. On EDD14, prior to MRI the eggs were cooled down for 60–70 min at 6 °C to minimize motion artifacts.[37] After cooling down, parafilm was removed, and N = 5 eggs were injected with citrate solution with air-oxidized DND (50 µL of 0.625 mM solution, equivalent to 20 mg kg^{-1} egg), N = 5 with gadobutrol (50 µL of 30 mM solution, N = 5), and N = 5 control eggs were not injected with anything. A chorioallantoic membrane blood vessel was injected under the microscope (Stemi 508, Zeiss Germany) using 34 G (TSK Laboratory International, Japan). MRI was performed immediately afterwards, at 24 h and 48 h post injections. A T_1-weighted gradient recalled echo sequence was

© 2023 The Authors. Advanced Materials published by Wiley-VCH GmbH

15214095, 2024, 11, Downloaded from https://onlinelibrary.wiley.com/doi/10.1002/adma.202310109 by Koc University, Wiley Online Library on [23/03/2024]. See the Terms and Conditions (https://onlinelibrary.wiley.com/terms-and-conditions) on Wiley Online Library for rules of use; OA articles are governed by the applicable Creative Commons License

used (TR/TE = 250/4.3 ms, 125 × 125 μm^2 in-plane resolution, 1 mm slice thickness, NEX = 8, 13 min 20 s total imaging time).

Macrophage Imaging with MRI: Macrophages were incubated for 24 h with addition of 1.25 µM and 2.5 µM air-oxidized DNDs in medium. Prior to MRI, incubated cells were washed three times with PBS, counted, and gently strained using a 1 µm membrane strainer (Pluriselect-USA Inc., USA) to separate DND particles that were not uptaken by macrophages. To aid easier visualization of macrophages, a membrane was protected with a tape (Tesa, Germany), where the cross-shaped area was cut out using a laser cutter (LPKF Laser and electronics AG, Germany). The media with cells that went through the strainer was counted again in order to correct for a number of macrophages left on the membrane. The membrane was gently cut from the strainer and embedded in 1% low melt agarose gel for MRI. Unlabelled macrophages and air-oxidized DND solution were treated the same way. A high-resolution MRI imaging was conducted using 3D RARE; TR/TE = 200/18.22 ms, 100^3 μm^3 resolution, NEX = 8, total time = 2 h 18 min.

Cytometric Bead Array (CBA): For cytokine secretion analysis, cells were seeded in 12-well plates and incubated for 24, 48 and 72 h with 1.25 µM DNDs, 2.5 µM DNDs, 0.1 µg mL^{-1} LPS or left untreated. Cell culture supernatants were taken at the respective time points and stored at −20 °C for cytokine analysis. Cytokine (IL-2, IL-4, IL-6, IL-10, IL-17α, IFN-γ, TNF-α) levels in cell culture supernatants were simultaneously measured using the BD cytometric bead array (CBA) mouse Th1/Th2/Th17 cytokine kit (BD Bioscience, USA). In brief, the assay kit provides a mixture of seven bead populations with distinct fluorescence intensities, which were coated with capture antibodies specific for the above listed cytokines. 50 µL of the mixed capture beads, 50 µL of the collected cell culture supernatant or standard dilution, and 50 µL of the mouse Th1/Th2/Th17 phycoerythrin (PE) detection reagent were added to each sample tube and incubated for 2 h at room temperature protected from light. The PE-conjugated detection antibodies then form sandwich complexes revealing the concentration of the respective cytokine by the PE fluorescence intensity. Subsequently, samples were washed and resuspended in washing buffer. Data acquisition was performed with a BD LSRFortessa X-20 (BD Bioscience, USA). The flow cytometry results were analyzed using FlowJo v10.8 Software (BD Life Sciences, USA) and cytokine concentrations were expressed in pg mL^{-1}. The experimental setup for CBA assay was repeated three times for all time points and conditions.

Statistical Analysis: All quantitative values are presented as mean ± standard deviation. All measurements including quantification were performed at least three times for each condition. Two-way ANOVA was used for CBA data analysis with Bonferroni post-hoc test, (P-value < 0.05 considered statistically significant). Origin was used for statistical analysis.

Supporting Information

Supporting Information is available from the Wiley Online Library or from the author.

Acknowledgements

This study was funded by the Max Planck Society. Authors would like to acknowledge Dr. Michael Beyerlein and Dr. Rolf Phmann for kind help with 3T and 14 T measurements, Peter Kopold for kind help with HRTEM, Dr. Elke Weiler for kind help with chicken embryos, and Dr. Yan Yu for her kind help with confocal microscopy. Schematic illustrations were created using BioRender (biorender.com).

Open access funding enabled and organized by Projekt DEAL.

Conflict of Interest

The authors declare no conflict of interest.

Author Contributions

J.L. designed the study and participated in experimental procedures, data collection, data analysis, and manuscript writing. E.G., A-M.W., P.S., J.L., G.W., and A.S. assisted with the experimental procedures and manuscript writing. M.S. participated in the study design, discussions, study supervision, and manuscript writing.

Data Availability Statement

The data that support the findings of this study are available from the corresponding author upon reasonable request.

Keywords

cell labelling, cell tracking, contrast agent, detonation nanodiamond, magnetic resonance imaging, nanodiamond, T1-weighted MRI

Received: September 29, 2023
Revised: November 24, 2023
Published online: December 14, 2023

[1] a) V. N. Mochalin, A. Pentecost, X.-M. Li, I. Neitzel, M. Nelson, C. Wei, T. He, F. Guo, Y. Gogotsi, *Mol. Pharmaceutics* **2013**, *10*, 3728; b) E. K. Chow, X.-Q. Zhang, M. Chen, R. Lam, E. Robinson, H. Huang, D. Schaffer, E. Osawa, A. Goga, D. Ho, *Sci. Transl. Med.* **2011**, *3*, 73ra21.

[2] a) X.-Q. Zhang, M. Chen, R. Lam, X. Xu, E. Osawa, D. Ho, *ACS Nano* **2009**, *3*, 2609; b) Z. Chu, K. Miu, P. Lung, S. Zhang, S. Zhao, H.-C. Chang, G. Lin, Q. Li, *Sci. Rep.* **2015**, *5*, 11661.

[3] a) G. Kucsko, P. C. Maurer, N. Y. Yao, M. Kubo, H. J. Noh, P. K. Lo, H. Park, M. D. Lukin, *Nature* **2013**, *500*, 54; b) S. Steinert, F. Ziem, L. T. Hall, A. Zappe, M. Schweikert, N. Götz, A. Aird, G. Balasubramanian, L. Hollenberg, J. Wrachtrup, *Nat. Commun.* **2013**, *4*, 1607.

[4] a) Q. Zhang, V. N. Mochalin, I. Neitzel, I. Y. Knoke, J. Han, C. A. Klug, J. G. Zhou, P. I. Lelkes, Y. Gogotsi, *Biomaterials* **2011**, *32*, 87; b) Q. Zhang, V. N. Mochalin, I. Neitzel, K. Hazeli, J. Niu, A. Kontsos, J. G. Zhou, P. I. Lelkes, Y. Gogotsi, *Biomaterials* **2012**, *33*, 5067.

[5] a) T.-J. Wu, Y.-K. Tzeng, W.-W. Chang, C.-A. Cheng, Y. Kuo, C.-H. Chien, H.-C. Chang, J. Yu, *Nat. Nanotechnol.* **2013**, *8*, 682; b) N. Mohan, C.-S. Chen, H.-H. Hsieh, Y.-C. Wu, H.-C. Chang, *Nano Lett.* **2010**, *10*, 3692.

[6] a) M. Rogosnitzky, S. Branch, *BioMetals* **2016**, *29*, 365; b) K. M. Hasebroock, N. J. Serkova, *Expert Opin. Drug Metab. Toxicol.* **2009**, *5*, 403; c) FDA Drug Safety Podcast: FDA warns that gadolinium-based contrast agents (GBCAs) are retained in the body; requires new class warnings, https://www.fda.gov/drugs/fda-drug-safety-podcasts/fda-drug-safety-podcast-fda-warns-gadolinium-based-contrast-agents-gbcas-are-retained-body-requires, (accessed: September 2023).

[7] M. Jeon, M. V. Halbert, Z. R. Stephen, M. Zhang, *Adv. Mater.* **2021**, *33*, 1906539.

[8] J. Zeng, L. Jing, Y. Hou, M. Jiao, R. Qiao, Q. Jia, C. Liu, F. Fang, H. Lei, M. Gao, *Adv. Mater.* **2014**, *26*, 2694.

[9] H. Wei, A. Wisniowska, J. Fan, P. Harvey, Y. Li, V. Wu, E. C. Hansen, J. Zhang, M. G. Kaul, A. M. Frey, G. Adam, A. I. Frenkel, M. G. Bawendi, A. Jasanoff, *Proc. Natl. Acad. Sci. USA* **2021**, *118*, 2102340118.

[10] L. M. Manus, D. J. Mastarone, E. A. Waters, X.-Q. Zhang, E. A. Schultz-Sikma, K. W. Macrenaris, D. Ho, T. J. Meade, *Nano Lett.* **2010**, *10*, 484.

[11] N. Rammohan, K. W. Macrenaris, L. K. Moore, G. Parigi, D. J. Mastarone, L. M. Manus, L. M. Lilley, A. T. Preslar, E. A. Waters, A. Filicko, C. Luchinat, D. Ho, T. J. Meade, *Nano Lett.* **2016**, *16*, 7551.

© 2023 The Authors. Advanced Materials published by Wiley-VCH GmbH

15214095, 2024, 11, Downloaded from https://onlinelibrary.wiley.com/doi/10.1002/adma.202310109 by Koc University, Wiley Online Library on [23/03/2024]. See the Terms and Conditions (https://onlinelibrary.wiley.com/terms-and-conditions) on Wiley Online Library for rules of use; OA articles are governed by the applicable Creative Commons License

[12] D. E. J. Waddington, M. Sarracanie, H. Zhang, N. Salameh, D. R. Glenn, E. Rej, T. Gaebel, T. Boele, R. L. Walsworth, D. J. Reilly, M. S. Rosen, *Nat. Commun.* **2017**, *8*, 15118.
[13] Y. Bao, J. A. Sherwood, Z. Sun, *J. Mater. Chem. C* **2018**, *6*, 1280.
[14] T. Gaebel, C. Bradac, J. Chen, J. M. Say, L. Brown, P. Hemmer, J. R. Rabeau, *Diamond Relat. Mater.* **2012**, *21*, 28.
[15] S. Stehlik, M. Varga, M. Ledinsky, D. Miliaieva, H. Kozak, V. Skakalova, C. Mangler, T. J. Pennycook, J. C. Meyer, A. Kromka, B. Rezek, *Sci. Rep.* **2016**, *6*, 38419.
[16] L. A. Bursill, A. L. Fullerton, L. N. Bourgeois, *Int. J. Mod. Phys. B* **2001**, *15*, 4087.
[17] a) P. I. Belobrov, S. K. Gordeev, É. A. Petrakovskaya, O. V. Falaleev, *Dokl. Phys.* **2001**, *46*, 459; b) V. Y. Osipov, A. I. Shames, T. Enoki, K. Takai, M. Endo, Y. Kaburagi, A. Y. Vul', *Diamond Relat. Mater.* **2010**, *19*, 492; c) A. I. Shames, V. Y. Osipov, H. J. von Bardeleben, A. Ya Vul', *J. Phys.: Condens. Matter* **2012**, *24*, 225302.
[18] V. Y. Osipov, A. I. Shames, T. Enoki, K. Takai, M. V. Baidakova, A. Y. Vul', *Diamond Relat. Mater.* **2007**, *16*, 2035.
[19] S. Kaciulis, *Surf. Interface Anal.* **2012**, *44*, 1155.
[20] H.-W. Tien, Y.-L. Huang, S.-Y. Yang, J.-Y. Wang, C.-C. M. Ma, *Carbon* **2011**, *49*, 1550.
[21] J. C. Lascovich, R. Giorgi, S. Scaglione, *Appl. Surf. Sci.* **1991**, *47*, 17.
[22] D. J. Morgan, *C – J. Carbon Res.* **2021**, *7*, 51.
[23] M. Smith, L. Scudiero, J. Espinal, J.-S. Mcewen, M. Garcia-Perez, *Carbon* **2016**, *110*, 155.
[24] S. Tanuma, C. J. Powell, D. R. Penn, *Surf. Interface Anal.* **1994**, *21*, 165.
[25] a) A. I. Shames, A. M. Panich, W. Kempiński, A. E. Alexenskii, M. V. Baidakova, A. T. Dideikin, V. Y. Osipov, V. I. Siklitski, E. Osawa, M. Ozawa, A. Y. Vul, *J. Phys. Chem. Solids* **2002**, *63*, 1993. b) A. M. Panich, A. I. Shames, H.-M. Vieth, E. Osawa, M. Takahashi, A. Y. Vul, *EPJ B* **2006**, *52*, 397.
[26] H. Wei, O. T. Bruns, M. G. Kaul, E. C. Hansen, M. Barch, A. Wisniowska, O. Chen, Y. Chen, N. Li, S. Okada, J. M. Cordero, M. Heine, C. T. Farrar, D. M. Montana, G. Adam, H. Ittrich, A. Jasanoff, P. Nielsen, M. G. Bawendi, *Proc. Natl. Acad. Sci. U. S. A.* **2017**, *114*, 2325.
[27] M. Longmire, P. L. Choyke, H. Kobayashi, *Nanomedicine* **2008**, *3*, 703.
[28] Wahajuddin. Arora, *Int. J. Nanomed.* **2012**, *7*, 3445.
[29] J. Bourquin, A. Milosevic, D. Hauser, R. Lehner, F. Blank, A. Petri-Fink, B. Rothen-Rutishauser, *Adv. Mater.* **2018**, *30*, 1704307.
[30] Y. X. Wang, *Quant. Imaging Med. Surg.* **2011**, *1*, 35.
[31] a) J. W. M. Bulte, J. Vymazal, R. A. Brooks, C. Pierpaoli, J. A. Frank, *J. Magn. Reson. Imaging* **1993**, *3*, 641; b) T.-C. Yeh, W. Zhang, S. T. Ildstad, C. Ho, *Magn. Reson. Med.* **1995**, *33*, 200.
[32] E. T. Ahrens, R. Flores, H. Xu, P. A. Morel, *Nat. Biotechnol.* **2005**, *23*, 983.
[33] A. D. Sherry, M. Woods, *Annu. Rev. Biomed. Eng.* **2008**, *10*, 391.
[34] E. T. Ahrens, J. W. M. Bulte, *Nat. Rev. Immunol.* **2013**, *13*, 755.
[35] L. Moore, J. Yang, T. T. H. Lan, E. Osawa, D.-K. Lee, W. D. Johnson, J. Xi, E. K.-H. Chow, D. Ho, *ACS Nano* **2016**, *10*, 7385.
[36] A. M. Schrand, L. Dai, J. J. Schlager, S. M. Hussain, E. Osawa, *Diamond Relat. Mater.* **2007**, *16*, 2118.
[37] M. M. Bain, A. J. Fagan, J. M. Mullin, I. Mcnaught, J. Mclean, B. Condon, *J. Magn. Re.son. Imaging* **2007**, *26*, 198.

© 2023 The Authors. Advanced Materials published by Wiley-VCH GmbH

15214095, 2024, 11, Downloaded from https://onlinelibrary.wiley.com/doi/10.1002/adma.202310109 by Koc University, Wiley Online Library on [23/03/2024]. See the Terms and Conditions (https://onlinelibrary.wiley.com/terms-and-conditions) on Wiley Online Library for rules of use; OA articles are governed by the applicable Creative Commons License